

# FAST CONVERGING LIDAR-AIDED PRECISE POINT POSITIONING: A CASE STUDY WITH LOW-COST GNSS

J. Zhang<sup>1\*</sup>, K. Khoshelham<sup>1</sup>, A. Khodabandeh<sup>1</sup>

<sup>1</sup> Department of Infrastructure Engineering, The University of Melbourne, Parkville, Victoria, Australia  
(junjiez@student., k.khoshelham@, akhodabandeh@)unimelb.edu.au

**KEY WORDS:** Extended Kalman-Filter (EKF), GNSS, Lidar, Low-cost, Real-time Precise Point Positioning (RT-PPP), Sensor fusion, Vehicle positioning.

## ABSTRACT:

With the growing interest in autonomous driving, accurate vehicle positioning remains an open problem, especially in urban environments. According to regulatory organisations, the vehicle positioning accuracy is required to be centimetre-level. As the most used positioning technique which provides globally referenced positioning solutions, GNSS is the fundamental component for realising real-time vehicle positioning, usually through the RTK approach. However, RTK requires a nearby reference station to enable integer ambiguity resolution for the ultra-precise carrier phase observations. In comparison, PPP makes use of State-Space Representation (SSR) corrections produced by global networks for satellite orbits and clocks to facilitate phase-based positioning. Moreover, IGS now offers Real-Time Service (RTS) to transmit such corrections. Notably, the major drawback of PPP is that it takes a long time to converge to precise solutions due to the carrier phase ambiguities being real-valued, which can be severely elongated when real-time corrections and low-cost GNSS receivers are used. In this paper, a tightly coupled positioning method is proposed, which shortens RT-PPP convergence to seconds by using lidar measurements referenced from an HD map through deep learning. The lidar measurements are generated by point cloud registration and weighted by their intensity values and geometric distributions, and are then combined with RT-PPP in an Extended Kalman-Filter (EKF), thus achieving fast convergence. Experimental results show that the proposed method achieves and maintains centimetre-level accuracy within 2 seconds using a low-cost UBLOX F9P receiver, which is a significant improvement as compared to the decimetre-level accuracy obtained from standalone RT-PPP.

## 1. INTRODUCTION

The realisation of autonomous driving systems relies on continuously accurate vehicle positioning, especially in urban environments (Zhang, 2022). Specifically, the positioning accuracy required by vehicles desiring to be maintained within their respective lanes is in the range of centimetres, while such performance should be consistent throughout the vehicle operations (Reid et al., 2019). By utilising Global Navigation Satellite Systems (GNSS), real-time kinematic (RTK) is the mostly commonly used precise positioning technique. RTK makes use of the ultra-precise carrier phase observations through integer ambiguity resolution by double-differencing the measurements with a nearby reference station (Teunissen and Montenbruck, 2017). However, such reference stations are not always available. In comparison, precise point positioning (PPP) employs State-Space Representation (SSR) corrections produced by global networks for satellite orbits and clocks to facilitate phase-based positioning, in which the positioning user needs only a single receiver (Zumberge et al., 1997). PPP has traditionally been used in a post-processing manner as the most accurate correction products can take roughly two weeks to be produced (IGS, 2019, BKG, 2021). Fortunately, International GNSS Service (IGS) now offers Real-Time Service (RTS) to provide corrections to enable real-time PPP (RT-PPP) (Caissy et al., 2013), which can be used for vehicle positioning. Several studies have analysed the performance of IGS RTS and concluded that its products of satellite orbit and clock corrections have accuracy and latency comparable as commercial and post-processed IGS counterparts (Elsobeiy and Al-Harbi, 2016, Al-

kan et al., 2020).

Nevertheless, like post-processed PPP, RT-PPP is notoriously disadvantaged by a long convergence time, which could exceed 30 minutes to reach decimetre-level accuracy, especially when it is used in the kinematic mode (Teunissen and Montenbruck, 2017, Choy et al., 2017). Here, we follow the classical definition that PPP convergence is declared when all of East-North-Up (ENU) errors are below 10 cm. This is caused by the fact that integer ambiguity resolution cannot be enabled for PPP due to un-modelled ionospheric delays and hardware biases (Teunissen, 1997). The positioning performance is even worse for low-cost GNSS receivers and/or antennas, as they offer noisier observations than those of survey-grade equipment (Nasr-Azadani et al., 2023). For autonomous systems, which often employ such devices and operate in multipath-heavy environments, the positioning accuracy and convergence time can be degraded to decimetres and over one hour, respectively (Gill et al., 2017).

Apart from PPP-RTK, which attempts to solve this problem by integer ambiguity resolution using additional corrections (Teunissen and Khodabandeh, 2015), multi-sensor integration has been investigated to improve the performance of PPP. As a common sensor used for environmental perception seen on-board of modern vehicles, light detection and ranging (lidar) scanners have been employed to compliment GNSS in various ways. First, lidar is most frequently applied for multipath mitigation, often in conjunction with high-definition (HD) maps containing geospatial information of the road surroundings (Wen et al., 2019, Groves et al., 2013). Second, it has been utilised to enable integer ambiguity resolution in RTK. For instance, a lidar-

\* Corresponding author.

aided instantaneous ambiguity resolution method was presented in (Zhang et al., 2022) which achieved the ambiguity success rate of 100% using single-system single-frequency observations. Finally, numerous studies have shown the effectiveness of lidar measurements for speeding up the convergence of PPP by successive scan matching (Li et al., 2021a, Li et al., 2021b, Li et al., 2022). However, existing methods rely on extracting and matching handcrafted geometric features from lidar points clouds, which are not robust in dynamic environments and can result in accumulated errors and low positioning accuracy.

In this work, we present a case study of combining RT-PPP with learning-based, map-aided lidar to realise an observation-level integration that continuously achieves high positioning accuracy within minimal convergence time, with an emphasis on the utilisation of a low-cost GNSS receiver. The lidar measurements are obtained from point cloud registrations between the online scans and a pre-built HD map by way of deep learning, which are then integrated with their dual-frequency PPP (DF-PPP) counterparts collected using a UBLOX F9P receiver in an Extended Kalman-Filter (EKF). The GNSS observations are corrected by IGS RTS products and the lidar measurements are innovatively weighted according to their intensity values and geometric distributions. The EKF also employs a constant-velocity model in its time-update to capture the vehicle's dynamics.

The remainder of this paper proceeds as follows. Section 2 discusses the mathematical details of the proposed PPP-Lidar integration. Section 3 presents the data collection configurations and the kinematic trajectory simulation used for the experiment, followed by the experimental results and discussion in Section 4. Finally, concluding remarks are drawn in Section 5.

## 2. METHODOLOGY

### 2.1 System overview

Figure 1 exhibits the overview of the proposed PPP-Lidar integrated positioning method, which tightly couples lidar and DF-PPP, i.e., their measurements are integrated directly, in an EKF using the constant-velocity model as the time-update. The lidar measurements are generated by registering rover scans (i.e., those collected by the lidar sensor on-board of the vehicle) with the reference scans from a pre-built, globally referenced HD map. The point cloud registration is performed by matching keypoints with similar features computed using a deep neural network. Such lidar measurements are fused with ionosphere-unknown DF-PPP observations in the measurement-update of the EKF, which assumes that the vehicle's velocity remains constant on average within a short period of time with a level of uncertainty in the time-update.

In this paper, we assume that the GNSS and lidar sensors installed on the vehicle have been pre-calibrated. In other words, their measurements are referenced to the same point that represents the vehicle position.

### 2.2 Lidar measurement generation

The lidar measurements are generated with respect to a pre-built HD map of the road environment. In this study, the map takes the form of 3D point clouds whose coordinates are georeferenced to the Earth-centred, Earth-fixed (ECEF) ITRF2014

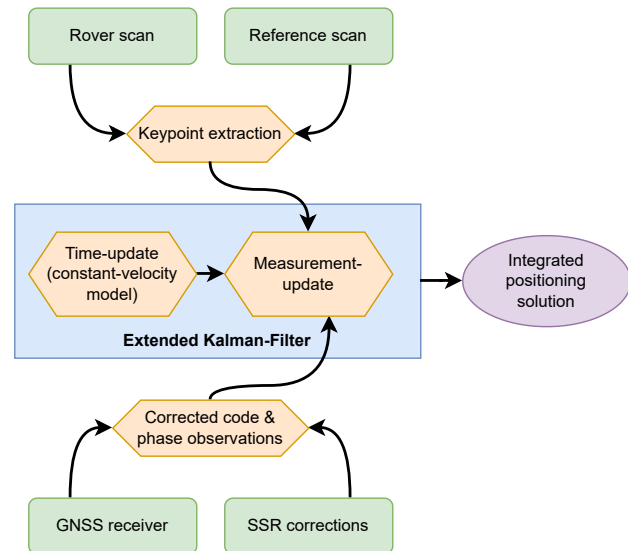


Figure 1. System overview of the proposed PPP-Lidar integrated positioning method.

frame and downsampled by the voxel size of 0.2 m. When a rover scan is collected by the lidar sensor in its own local frame whose origin is the vehicle position, a nearby reference scan is selected from the HD map for registration. A deep learning framework named MS-SVConv (Horache et al., 2021) is pre-trained and then used to compute multi-dimensional features for the points in both rover and reference scans. Matching keypoints between the two are found as nearest neighbours in terms of the Euclidean norms of such features, after which outliers are identified and removed by using random sample consensus (RANSAC) to estimate a transformation from the local coordinates of the keypoints to their global counterparts (Fischler and Bolles, 1981). This estimated transformation consists of a  $3 \times 3$  rotation matrix  $R$  and a Cartesian translation vector  $x_r$  that corresponds with the vehicle position. Therefore, the observation equation for  $n$  matching keypoints at the same epoch reads as follows

$$[I_n \otimes R][y_L - e_L] + \mathbf{1}_{n \times 1} \otimes x_r = c \quad (1)$$

where  $\otimes$  denotes the Kronecker product (Henderson et al., 1983) and  $\mathbf{1}$  represents a matrix of ones.  $y_L$  and  $e_L$  contain the local coordinates of the keypoints and their measurement residuals, respectively, concatenated into column vectors, while their corresponding global coordinates obtained from the reference scan are denoted as the column vector  $c$ .

### 2.3 PPP observation equations

The proposed positioning method adopts the DF-PPP model with ionospheric delays as unknown parameters to estimate. Assuming that a priori PPP corrections and precise products for satellite orbits and clocks have been applied (Kouba and Héroux, 2001), except the receiver phase centre offset and variation corrections as they are not provided for low-cost equipment, for receiver  $r$  tracking  $m$  satellites on frequency  $j$  ( $j = 1, 2$ ), the linearised GNSS code and carrier phase observation equations can be written as

$$\begin{cases} \Delta p_{r,j} = \mathbf{G}_r \Delta \mathbf{x}_r + \mathbf{1}_{m \times 1} dt_r + \mu_j \mathbf{t}_r + \mathbf{e}_{p,j} \\ \Delta \phi_{r,j} = \mathbf{G}_r \Delta \mathbf{x}_r + \mathbf{1}_{m \times 1} dt_r - \mu_j \mathbf{t}_r + \lambda_j \mathbf{a}_{r,j} + \mathbf{e}_{\phi,j} \end{cases} \quad (2)$$

in which  $\Delta p_{r,j}$  and  $\Delta \phi_{r,j}$  are the observed-minus-computed code and carrier phase observations, respectively.  $\mathbf{G}_r$  contains the satellite-to-receiver direction unit vectors.  $dt_r$ ,  $\mathbf{t}_r$  and  $\mathbf{a}_{r,j}$  denote the estimable receiver clock, ionospheric delays for the first frequency and real-valued ambiguities including the phase biases.  $\lambda_j$  is the wavelength of frequency  $j$ , while  $\mu_j = \lambda_j^2 / \lambda_1^2$ . Finally,  $\mathbf{e}_{p,j}$  and  $\mathbf{e}_{\phi,j}$  represent the code and phase measurement residuals. All parameters have units of length, except  $\mathbf{a}_{r,j}$  which is expressed in cycles. Since (1) and (2) share the unknown vehicle position  $\mathbf{x}_r$ , they can be directly integrated in an EKF to estimate this parameter.

## 2.4 EKF formulation

The full implementation details of this EKF formulation can be found in our previous work (Zhang et al., 2023). First, the time-update of the EKF integration provides a prediction of the ambiguities  $\mathbf{a}_{r,j}$  and the vehicle position  $\mathbf{x}_r$ . While the former is kept constant over time unless cycle slips are detected, the vehicle position is predicted by assuming the velocity is unchanged from the previous epoch, with its acceleration vector modelled by a zero-mean white-noise vector with specified spectral densities. The mathematical derivation of such constant-velocity model can be found in (Teunissen, 2001).

Next, the measurement-update of the EKF combines the lidar and PPP observations, if they are present, with the time-updated solution in a Weighted Least Squares (WLS) manner to yield the estimated position. The weights of the GNSS code, carrier phase and lidar measurements, respectively, are determined as the inverse of their variances as follows

$$\begin{cases} \sigma_{p_r^s}^2 = \sigma_p^2 / \sin^2 \theta_s \\ \sigma_{\phi_r^s}^2 = \sigma_\phi^2 / \sin^2 \theta_s \\ \sigma_{x_i}^2 = \sigma_{y_i}^2 = \sigma_{z_i}^2 = [a \times \gamma_i^b]^2 \end{cases} \quad (3)$$

where  $\sigma_{p_r^s}^2$  and  $\sigma_{\phi_r^s}^2$  are the variances of GNSS code and carrier phase observations between receiver  $r$  and satellite  $s$ , respectively.  $\sigma_p$  and  $\sigma_\phi$  are empirically determined standard deviations of these two measurements types at zenith, while  $\theta_s$  is the elevation angle of satellite  $s$ . Therefore, the higher the elevation of a satellite, the smaller its variances of measurements. On the other hand,  $\sigma_{x_i}^2 = \sigma_{y_i}^2 = \sigma_{z_i}^2$  indicate that the three coordinates of lidar keypoint  $i$  have uniform variances computed using its intensity value  $\gamma_i$ , with  $a$  and  $b$  being empirical constants varying by the lidar sensor model (Wujanz et al., 2017). In other words, the higher the intensity of a lidar keypoint, the smaller its variances.

Moreover, due to RANSAC randomly selecting a subset of the points for estimating the transformation between rover and reference scans, it is possible for it to yield an incorrect result which is hard to detect. This often occurs when the keypoints are clustered (Zhang et al., 2021). Using Figure 2 as an example, the green points are well distributed around the lidar sensor (blue cross), while the red points are clustered in one direction, possibly leading to an inaccurate extraction of keypoints through RANSAC. To mitigate the effect of such inappropriate distributions of keypoints, we apply the Position Dilution of

Precision (PDOP) indicator well known in GNSS to lidar keypoints as follows (Srinara and Chiu, 2022)

$$\text{PDOP}_L = \sqrt{\text{tr}([\mathbf{G}_L^T \mathbf{G}_L]^{-1})} \quad (4)$$

where  $\text{tr}(\cdot)$  refers to the trace of a matrix. For  $n$  keypoints extracted per epoch via MS-SVConv and RANSAC,  $\mathbf{G}_L$  denotes a  $n \times 3$  matrix formed by the unit direction vectors between the keypoints and the lidar sensor. As a result,  $\text{PDOP}_L$  is a scalar that indicates to what degree the keypoints are clustered. This value is used to scale the part of the weight matrix corresponding to the lidar measurements. In other words, the more clustered the keypoints, the smaller weights they are given in the measurement-update.

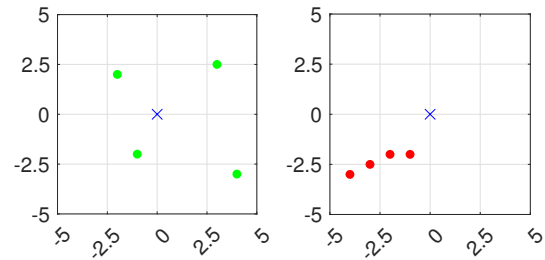


Figure 2. Examples of distributions of lidar keypoints. The green dots represent a geometrically appropriate distribution of extracted lidar keypoints and the red dots represent clustered keypoints.

## 3. EXPERIMENTAL EVALUATION

### 3.1 GNSS data collection

A simulated kinematic experiment was conducted to evaluate the positioning performance of the discussed integration of DF-PPP and lidar. The GNSS data were collected at 1 Hz using low-cost GNSS devices, namely UBLOX F9P receiver and UBLOX ANN-MB antenna on Parkville campus of The University of Melbourne, Australia on 04 August 2022 (UBLOX, 2022b, UBLOX, 2022a). The antenna was installed on a levelled tripod occupying a stationary point in an open-sky environment, as displayed in Figure 3. As a result, 12 one-hour samples were collected along with real-time precise products for satellite orbit and clock corrections from the IGS RTS SSRA01IGS1 stream (formerly IGS01) recorded simultaneously at the sampling rate of 10 s using BKG Ntrip Client (IGS, 2022). On average, 8 valid GPS satellites with L1 and L2 observations were tracked throughout the operation.

### 3.2 Lidar data and trajectory simulation

The lidar data used in the simulated experiment were acquired from sequence 00 of the KITTI dataset, whose lidar data were generated using a Velodyne HDL-64E scanner installed on a moving vehicle (Geiger et al., 2013). Figure 4 exhibits the ground truth trajectory of this vehicle. The point clouds were separated into equal numbers of rover and reference scans (HD map). For every rover scan, at 1 Hz, an overlapped reference scan is selected with the approximate distance of 10 m and downsampled. In total, 3600 pairs of scans were formed over the duration of 1 hour.

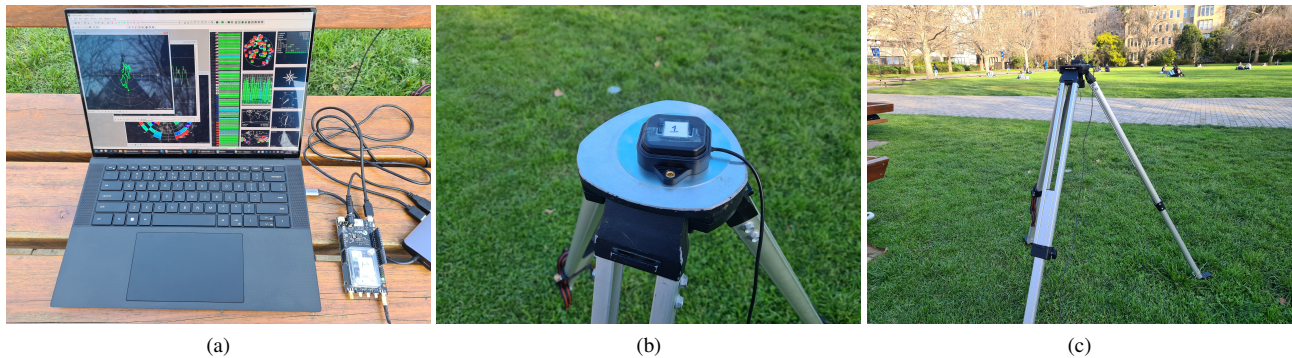


Figure 3. GNSS data collection setup using UBLOX F9P receiver, UBLOX ANN-MB antenna and a laptop computer with U-Center software. (a) Laptop running U-Center and UBLOX F9P receiver. (b) ANN-MB antenna. (c) Tripod on which the antenna is installed.

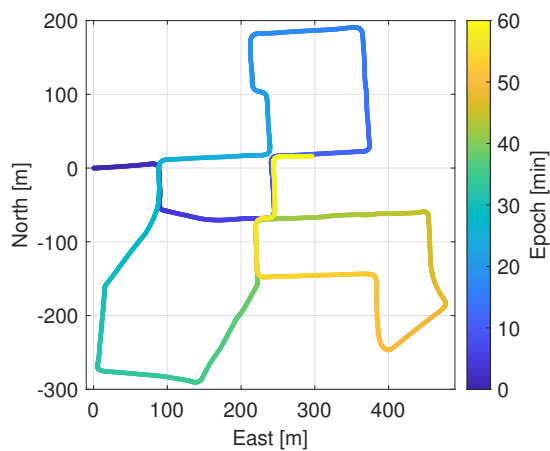


Figure 4. 1-hour trajectory obtained from sequence 00 of KITTI dataset.

Since the GNSS and lidar data had been obtained from different sources, they needed to be simulated onto the same trajectory as shown in Figure 4. The point coordinates of the reference scans in the HD map were transformed so that the starting point corresponded with the stationary point on which the GNSS antenna was held. In addition, the GNSS observations at every epoch were also transformed using the ground truth coordinates of the vehicle in the way that the antenna’s position would be moving along the trajectory, so that both GNSS and lidar measurements were synced and referenced from the same kinematic point representing the vehicle.

## 4. RESULTS AND DISCUSSION

### 4.1 Keypoint extraction results

Before examining the positioning performance of the proposed method, we begin with results of the lidar keypoint extraction stage and a validation of the lidar measurement weighting strategy. The deep neural network MS-SVConv was pre-trained using ETH dataset (Pomerleau et al., 2012) before being utilised for feature computations on the KITTI lidar data used in the experiment. The constants  $a$  and  $b$  in (3) are empirically determined as 0.03 and -1, respectively. As a result, keypoints are successfully matched and extracted from 3105/3600 pairs of rover and reference scans, giving the keypoint matching success rate of 86.3%. Figure 5 shows the number of lidar keypoints per

epoch, which indicates that 16 keypoints are generated on average.

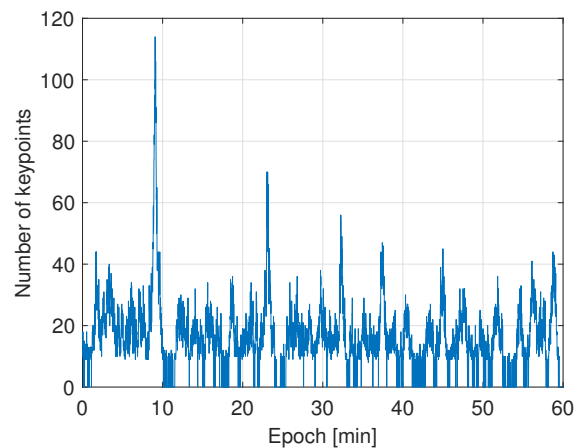


Figure 5. Number of successfully matched lidar keypoints per epoch.

To verify the advantage of scaling the weights of lidar measurements by  $PDOP_L$  in the measurement-update of the EKF, positioning is performed using the proposed method utilising only the time-update and the extracted lidar keypoints as measurements (i.e., no GNSS observation is involved), with (4) applied and not. In the constant-velocity model, the ENU spectral densities dictating the process noise in the time-update are computed as 0.05, 0.05 and  $0.03 \text{ m}^2/\text{s}^3$ , respectively, based on the ground truth acceleration of the vehicle. Figure 6 displays the improvement of 3D positioning accuracy by applying the weight scaling. It can be seen that despite occasional worsening of the accuracy, most epochs experience smaller positioning errors, with some improvements exceeding 2 m. This shows that (4) can effectively mitigate the effect of clustered lidar keypoints to achieve more appropriate measurement weighting in the EKF.

### 4.2 Positioning performance comparison

In this section, we evaluate the positioning performance of the proposed integration using low-cost GNSS equipment. The satellite cutoff angle is chosen as  $15^\circ$  and the standard deviations of code and carrier phase observations are specified as  $\sigma_p = 0.3 \text{ m}$  and  $\sigma_\phi = 0.003 \text{ m}$ , respectively, considering the measurement quality of the receiver and antenna used in the

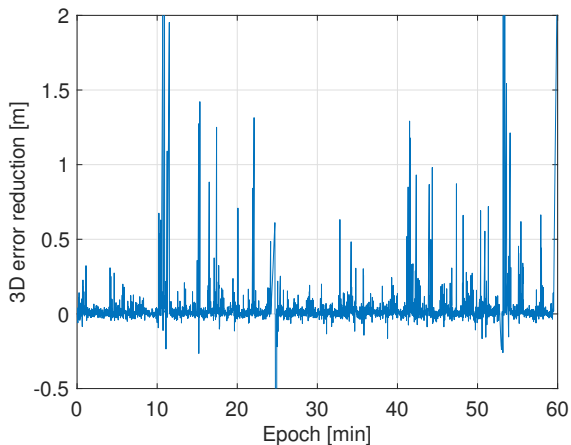


Figure 6. 3D error reduction after applying  $PDOP_L$  by estimating positions using lidar data only.

experiment. In addition, we recognise that the aforementioned keypoint matching success rate is idealistic and it can be much lower in reality due to outdated or sparse HD map. Therefore, to also test the proposed method's reliance on lidar input, 3 positioning setups are compared:

1. PPP-only: the measurement-update uses only PPP observations;
2. PPP-Lidar (1s): the measurement-update uses PPP observations and all available lidar measurements;
3. PPP-Lidar (10s): the measurement-update uses PPP observations and lidar measurements are only available once every 10 s at most.

Table 1 exhibits the root mean squared errors (RMSE) and mean convergence time summarised from the 12 one-hour samples using these 3 positioning schemes. It is expected that PPP-only shows the worst performance overall, with the horizontal and 3D RMSE of 1.85 and 4.60 m, respectively, as well as the convergence time of over 1 hour, which are apparently inappropriate for vehicle positioning. In comparison, by combining with lidar, PPP-Lidar (1s) improves the horizontal RMSE to 10 cm, while its 3D counterpart is slightly beyond centimetre-level at 0.12 cm. More impressively, the convergence time is reduced to 1.8 s, which can be virtually considered eliminated, thanks to the high accuracy of lidar measurements. By limiting lidar input to once every 10 s, PPP-Lidar (10s) still achieves centimetre-level accuracy in the North and Up directions. However, the East RMSE is increased by 50% from that of PPP-Lidar (1s), while the 3D RMSE reaches 17 cm. The mean convergence time is also increased to 13.2 s, yet it is still significantly improved comparing with PPP-only. In addition, Figure 7 shows the cumulative distribution functions (CDF) of the positioning errors. It is evident that the proposed integration can dramatically improve positioning accuracy and remove large positioning errors as compared to classical PPP, while decreasing the frequency of lidar measurements only slightly degrades the positioning performance.

Taking a closer look at the PPP-only results, Figure 8 depicts the 25th quartile, median values and 75th quartile of the absolute ENU errors per epoch using this positioning method. It is shown that the positioning accuracy is not only very low, as

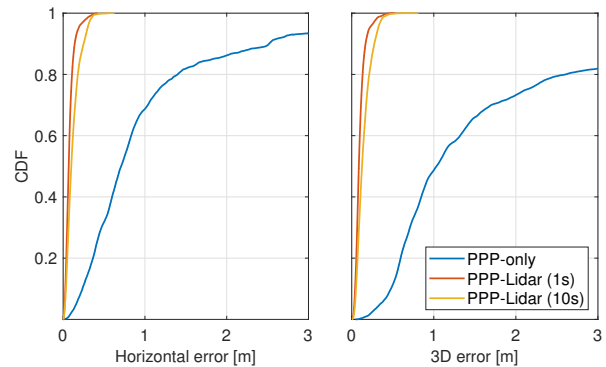


Figure 7. CDF of the horizontal and 3D positioning errors using PPP-only, PPP-Lidar (1s) and PPP-Lidar (10s).

centimetre-level accuracy is rarely reached, but also highly unstable. Specifically, despite the absolute errors reducing for the first 10 min, which is the expected behaviour as the precision of carrier phase ambiguities increases over time, they tend to diverge at later epochs. Moreover, the results from different samples are inconsistent as the dispersion between them (yellow region) can span over decimetres. Such poor positioning performance can be attributed to the low measurement quality of low-cost GNSS devices and the low accuracy of real-time PPP precise products, making standalone RT-PPP unsuitable for vehicle positioning.

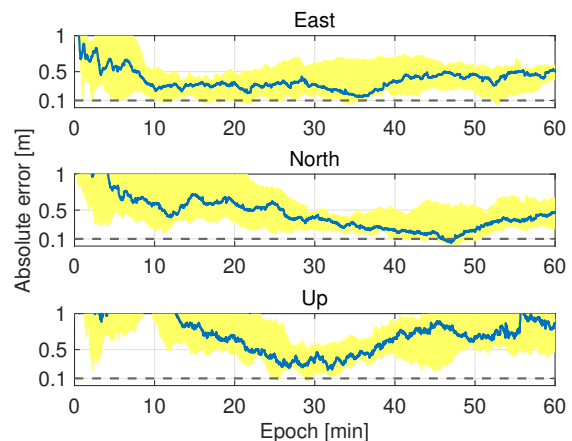


Figure 8. Median values (blue) and interquartile ranges (yellow) of absolute ENU positioning errors using PPP-only.

In contrast, the integration of lidar measurements significantly improves the positioning accuracy and convergence speed. Figure 9 shows the 25th quartile, median values and 75th quartile of the absolute ENU errors per epoch using PPP-Lidar (1s), with the green background indicating epochs with lidar input. It is reported that the ENU errors are at the centimetre-level immediately, essentially eliminating the PPP convergence time. Although the errors increase over 10 cm occasionally when lidar input is missing, the proposed method can successfully maintain centimetre-level accuracy for most of the epochs, showing promise for reliable lane-level vehicle positioning using low-cost GNSS equipment.

Lastly, Figure 10 shows the 25th quartile, median values and 75th quartile of the absolute ENU errors per epoch using PPP-Lidar (10s). Understandably, with less frequent lidar input, the convergence to centimetre-level positioning accuracy takes

Table 1. RMSE of positioning errors and mean convergence time. E, N, U, H represent East, North, Up and Horizontal errors, respectively.

Positioning method	RMSE [m]					Mean convergence time
	E	N	U	H	3D	
PPP-only	1.61	0.92	4.22	1.85	4.60	>1 h
PPP-Lidar (1s)	0.08	0.06	0.06	0.10	0.12	1.8 s
PPP-Lidar (10s)	0.12	0.08	0.09	0.15	0.17	13.2 s

## 5. CONCLUSION AND OUTLOOK

By way of conclusion, an observation-level integration of PPP and lidar as a vehicle positioning system is proposed and studied using low-cost GNSS equipment in this paper. The proposed method utilises the ionosphere-unknown DF-PPP model, whose observations are corrected by real-time precise products for satellite orbits and clocks, as well as lidar measurements generated by point cloud registration with a pre-built HD map using a deep neural network in an EKF, in which the time-update consists of a constant-velocity model that captures the vehicle motion.

The proposed method was evaluated in a simulated kinematic experiment in terms of positioning accuracy and convergence time using UBLOX F9P receiver and UBLOX ANN-MB antenna, as well as lidar data from KITTI dataset. Due to the low measurement quality of the GNSS equipment, classical PPP can only offer decimetre-level positioning accuracy, which is too poor for vehicle positioning. By combining PPP and lidar in the proposed method, centimetre-level accuracy can be immediately achieved and reliably maintained throughout the operation, effectively eliminating the need of convergence time. Moreover, to obtain fast convergence and near-centimetre-level positioning accuracy, the proposed integration only requires lidar input to be available once every 10 s.

On the other hand, we recognise that the experiment is a simulation that does not fully consider the dynamic conditions in urban environments that can negatively affect positioning performance, e.g., signal blockage and multipath. Future work can focus on a real-world kinematic experiment to assess the performance of the proposed positioning system. In addition, this method can be extended by utilising PPP-RTK corrections to perform integer ambiguity resolution for improved accuracy and convergence speed. Finally, other formats of HD maps such as occupancy grid maps can also be explored to decrease the difficulty and/or costs of producing HD maps.

## ACKNOWLEDGEMENTS

This research did not receive any specific grant from funding agencies in the public, commercial, or not-for-profit sectors. The first author acknowledges the financial support from The University of Melbourne through the Melbourne Research Scholarship.

## REFERENCES

Alkan, R. M., Erol, S., Ozulu, I. M., İlçi, V., 2020. Accuracy comparison of post-processed PPP and real-time absolute positioning techniques. *Geomatics, Natural Hazards and Risk*, 11(1), 178–190.

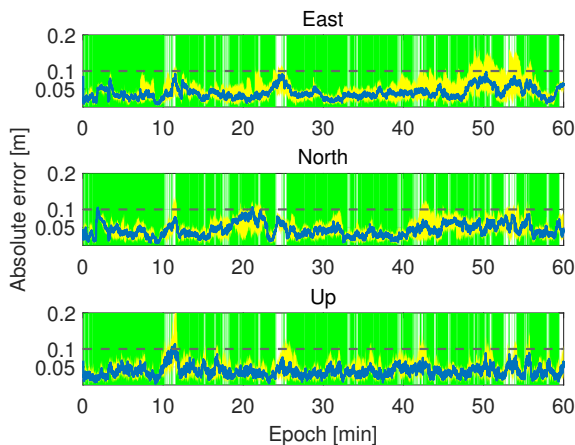


Figure 9. Median values (blue) and interquartile ranges (yellow) of absolute ENU positioning errors using PPP-Lidar (1s). Green background highlights epochs with lidar input.

slightly longer. However, we believe that a convergence time of less than 1 min is acceptable for vehicle positioning, considering that high accuracy can be maintained after this period, despite lidar measurements being unavailable for more than 90% of the epochs. It is shown that PPP-Lidar (10s) is sufficient for consistently achieving cm- or near-centimetre-level of positioning accuracy, except for the last 15 min when the errors exceed 10 cm due to low quality of GNSS observations, as can be seen in previous results as well.

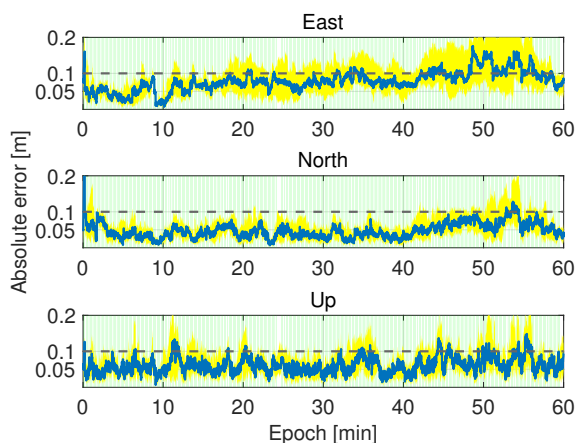


Figure 10. Median values (blue) and interquartile ranges (yellow) of absolute ENU positioning errors using PPP-Lidar (10s). Green background highlights epochs with lidar input.

- BKG, 2021. BKG Ntrip Client (BNC), Version 2.12. Federal Agency for Cartography and Geodesy. [igs.bkg.bund.de/ntrip/bnc](https://www.bkg.bund.de/ntrip/bnc) (04 August 2022).
- Caissy, M., Agrotis, L., Weber, G., Fisher, S., 2013. The IGS real-time service. *EGU General Assembly Conference Abstracts*, Vienna, Austria, EGU2013–11168.
- Choy, S., Bisnath, S., Rizos, C., 2017. Uncovering common misconceptions in GNSS Precise Point Positioning and its future prospect. *GPS Solutions*, 21(1), 13–22.
- Elsobeiey, M., Al-Harbi, S., 2016. Performance of real-time Precise Point Positioning using IGS real-time service. *GPS Solutions*, 20(3), 565–571.
- Fischler, M. A., Bolles, R. C., 1981. Random sample consensus: a paradigm for model fitting with applications to image analysis and automated cartography. *Communications of the ACM*, 24(6), 381–395.
- Geiger, A., Lenz, P., Stiller, C., Urtasun, R., 2013. Vision meets robotics: The KITTI dataset. *The International Journal of Robotics Research*, 32(11), 1231–1237.
- Gill, M., Bisnath, S., Aggrey, J., Seepersad, G., 2017. Precise point positioning (PPP) using low-cost and ultra-low-cost GNSS receivers. *Proceedings of the 30th International Technical Meeting of the Satellite Division of The Institute of Navigation (ION GNSS+ 2017)*, The Institute of Navigation, Portland, Oregon, 226–236.
- Groves, P. D., Jiang, Z., Rudi, M., Strode, P., 2013. A portfolio approach to NLOS and multipath mitigation in dense urban areas. *Proceedings of the 26th International Technical Meeting of the Satellite Division of The Institute of Navigation (ION GNSS+ 2013)*, The Institute of Navigation, Nashville, TN, 3231–3247.
- Henderson, H. V., Pukelsheim, F., Searle, S. R., 1983. On the History of the Kronecker Product. *Linear and Multilinear Algebra*, 14(2), 113–120.
- Horache, S., Deschaud, J.-E., Goulette, F., 2021. 3D point cloud registration with multi-scale architecture and unsupervised transfer learning. *2021 International Conference on 3D Vision (3DV)*, 1351–1361.
- IGS, 2019. IGS quality of service fact sheet. International GNSS Service. [files.igs.org/pub/resource/pubs/IGS\\_Quality\\_of\\_Service-131031.pdf](https://files.igs.org/pub/resource/pubs/IGS_Quality_of_Service-131031.pdf) (04 August 2022).
- IGS, 2022. RTS combination products. International GNSS Service. [igs.org/rtts/products](https://www.igs.org/rtts/products) (04 August 2022).
- Kouba, J., Héroux, P., 2001. Precise Point Positioning Using IGS Orbit and Clock Products. *GPS Solutions*, 5(2), 12–28.
- Li, S., Wang, S., Zhou, Y., Shen, Z., Li, X., 2022. Tightly coupled integration of GNSS, INS and LiDAR for vehicle navigation in urban environments. *IEEE Internet of Things Journal*, 1–1.
- Li, T., Pei, L., Xiang, Y., Wu, Q., Xia, S., Tao, L., Guan, X., Yu, W., 2021a. P3-LOAM: PPP/LiDAR Loosely Coupled SLAM With Accurate Covariance Estimation and Robust RAIM in Urban Canyon Environment. *IEEE Sensors Journal*, 21(5), 6660–6671.
- Li, X., Wang, H., Li, S., Feng, S., Wang, X., Liao, J., 2021b. GIL: a tightly coupled GNSS PPP/INS/LiDAR method for precise vehicle navigation. *Satellite Navigation*, 2(1), 26.
- Nasr-Azadani, S., Alizadeh, M. M., Schuh, H., 2023. Detecting multipath effects on smartphone GNSS measurements using CMCD and elevation-dependent SNR selection technique. *ISPRS Annals of the Photogrammetry, Remote Sensing and Spatial Information Sciences*, X-4-W1-2022, 595–602.
- Pomerleau, F., Liu, M., Colas, F., Siegwart, R., 2012. Challenging data sets for point cloud registration algorithms. *The International Journal of Robotics Research*, 31(14), 1705–1711.
- Reid, T. G. R., Houts, S. E., Cammarata, R., Mills, G., Agarwal, S., Vora, A., Pandey, G., 2019. Localization requirements for autonomous vehicles. *SAE International Journal of Connected and Automated Vehicles*, 2(3), 173–190.
- Srinara, S., Chiu, Y.-T., 2022. Adaptive covariance estimation of LiDAR-based positioning error for multi-sensor fusion scheme with autonomous vehicular navigation system. *Proceedings of the 35th International Technical Meeting of the Satellite Division of The Institute of Navigation (ION GNSS+ 2022)*, The Institute of Navigation, Denver, Colorado, 1650–1664.
- Teunissen, P. J. G., 1997. A canonical theory for short GPS baselines. Part II: the ambiguity precision and correlation. *Journal of Geodesy*, 71(7), 389–401.
- Teunissen, P. J. G., 2001. *Dynamic Data Processing; Recursive Least Squares*. VSSD.
- Teunissen, P. J. G., Khodabandeh, A., 2015. Review and principles of PPP-RTK methods. *Journal of Geodesy*, 89(3), 217–240.
- Teunissen, P. J. G., Montenbruck, O. (eds), 2017. *Springer handbook of global navigation satellite systems*. Springer.
- UBLOX, 2022a. ANN-MB series module product summary. UBLOX. [https://content.u-blox.com/sites/default/files/ANN-MB\\_ProductSummary\\_UBX-18047741.pdf](https://content.u-blox.com/sites/default/files/ANN-MB_ProductSummary_UBX-18047741.pdf) (04 August 2022).
- UBLOX, 2022b. ZED-F9P module product summary. UBLOX. [https://content.u-blox.com/sites/default/files/ZED-F9P\\_ProductSummary\\_UBX-17005151.pdf](https://content.u-blox.com/sites/default/files/ZED-F9P_ProductSummary_UBX-17005151.pdf) (04 August 2022).
- Wen, W., Zhang, G., Hsu, L.-T., 2019. Correcting NLOS by 3D LiDAR and building height to improve GNSS single point positioning. *Navigation*, 66(4), 705–718.
- Wujanz, D., Burger, M., Mettenleiter, M., Neitzel, F., 2017. An intensity-based stochastic model for terrestrial laser scanners. *ISPRS Journal of Photogrammetry and Remote Sensing*, 125, 146–155.
- Zhang, J., 2022. Lidar-aided instantaneous GNSS ambiguity resolution in challenging environments: Theoretical assessment and numerical results. *Proceedings of the 35th International Technical Meeting of the Satellite Division of The Institute of Navigation (ION GNSS+ 2022)*, The Institute of Navigation, Denver, Colorado, 2054–2063.
- Zhang, J., Khodabandeh, A., Khoshelham, K., 2022. Centimeter-level positioning by instantaneous lidar-aided GNSS ambiguity resolution. *Measurement Science and Technology*, 33(11), 115020.

Zhang, J., Khodabandeh, A., Khoshelham, K., 2023. On the role of lidar measurements in speeding up precise point positioning convergence. *GPS Solutions*, 27(3), 149.

Zhang, J., Khoshelham, K., Khodabandeh, A., 2021. Seamless Vehicle Positioning by Lidar-GNSS Integration: Standalone and Multi-Epoch Scenarios. *Remote Sensing*, 13(22), 4525.

Zumberge, J. F., Heflin, M. B., Jefferson, D. C., Watkins, M. M., Webb, F. H., 1997. Precise point positioning for the efficient and robust analysis of GPS data from large networks. *Journal of Geophysical Research: Solid Earth*, 102(B3), 5005–5017.